scientific reports

OPEN

A physicochemical model of X-ray induced photodynamic therapy (X-PDT) with an emphasis on tissue oxygen concentration and oxygenation

Farideh. S. Hosseini[1], Nadia Naghavi[1✉] & Ameneh Sazgarnia[2,3]

X-PDT is one of the novel cancer treatment approaches that uses high penetration X-ray radiation to activate photosensitizers (PSs) placed in deep seated tumors. After PS activation, some reactive oxygen species (ROS) like singlet oxygen ($^1O_2$) are produced that are very toxic for adjacent cells. Efficiency of X-PDT depends on $^1O_2$ quantum yield as well as X-ray mortality rate. Despite many studies have been modeled X-PDT, little is known about the investigation of tissue oxygen content in treatment outcome. In the present study, we predicted X-PDT efficiency through a feedback of physiological parameters of tumor microenvironment includes tissue oxygen and oxygenation properties. The introduced physicochemical model of X-PDT estimates $^1O_2$ production in a vascularized and non-vascularized tumor under different tissue oxygen levels to predict cell death probability in tumor and adjacent normal tissue. The results emphasized the importance of molecular oxygen and the presence of a vascular network in predicting X-PDT efficiency.

Cancer is the second cause of death in the world after cardiovascular disease[1]. Among the various methods proposed for cancer treatment, radiotherapy (RT) utilizes ionizing radiation to fatally damage tumor cells. High tissue penetration of X-rays induce DNA breaks, resulting efficient cancer cell destruction[2]. Simultaneously, ionizing radiation induce side effects for surrounding normal tissues[3]. So, it is a challenging problem to balance between inhibiting tumor growth and reducing side effects to normal tissue. To achieve this goal, the concept of therapeutic efficiency has been defined as the ratio of cell death in tumor to healthy tissue. There are different factors affect the efficiency of RT such as tissue morphological characteristics (includes tissue oxygenation, Cell division speed, …), nature of radiation (dose, linear energy transfer, …) and presence of substances that affect the cell response to radiation (like radiosesitizer and radioresistant agents)[4]. Among these, radiosensitizers are chemical agents increase lethal effects of radiation[5] and significantly lowering the radiation exposure necessary for tumor regression[6].

In contrast to RT, photodynamic therapy (PDT) is a relatively new cancer treatment approach utilizes intermediate energies of electromagnetic spectrum (optical radiation) to produce cytotoxic ROS[7]. PDT interactions need three components of oxygen, PS and light with an appropriate wavelength to damage cells[8]. In the absence of each component, PDT interactions will not initiate. Thus, PDT is recognized as a safe, low toxicity and highly selective method of cancer treatment[7]. However, PDT is restricted to accessible tissues due to limited penetration depth of light.

X-PDT, on the other hands, is a novel approach can be used for treatment of cancer[9]. X-PDT utilizes nanocomposites include some nanoscintillators to locally convert X-rays to optical luminescence and activate conjugated PSs. In presence of oxygen, the activated PS, generate ROS to damage cancer cells[8,10]. Therefore, there are two important factors that affect the efficiency of X-PDT: first, scintillator light yield transforming X-ray into light, and then efficiency of the emitted photons being absorbed by the PS.

Moreover, metallic nanoscintillators increase local dose by selectively scattering and absorbing X-rays causing localized damage to DNA[5,11]. As a result, X-PDT combines RT and PDT to improve therapeutic outcome

[1]Department of Electrical Engineering, Ferdowsi University of Mashhad, Mashhad, Iran. [2]Medical Physics Research Center, Mashhad University of Medical Sciences, Mashhad, Iran. [3]Department of Medical Physics, Faculty of Medicine, University of Medical Sciences, Mashhad, Iran. ✉email: nn.naghavi@gmail.com
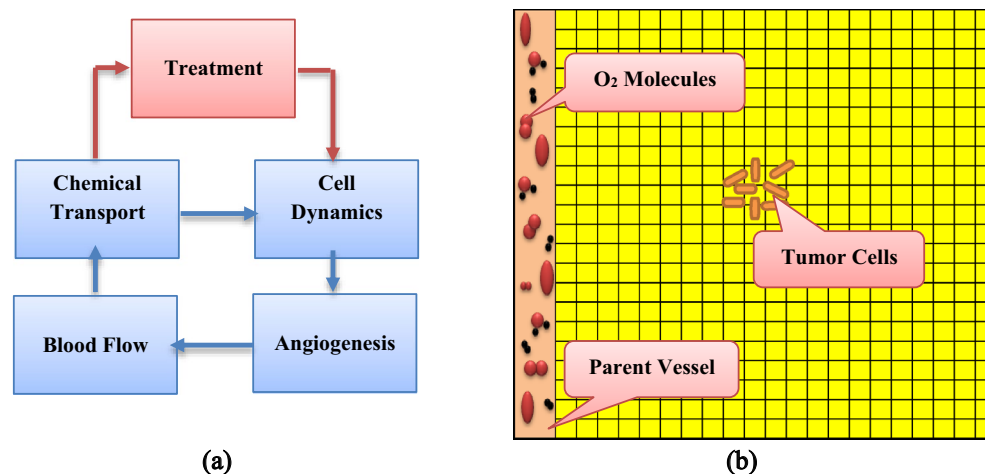
Figure 1. Overview of the model includes (**a**) Block diagram of the five compartment model and (**b**) Schematic of simulation space.

and reduces radiation damage to normal tissues[12]. X-PDT attacks both DNA and membrane of cancerous cells causing more effective damage than conventional RT or PDT alone[13]. With the growth of nanotechnology, the idea of using nanoscintillators for activating adjacent PSs introduced by Chen et al. in 2006[14]. Since then further efforts have been made by different researchers as reviewed in[9]. However, there are still some challenges for the clinical use of X-PDT[9] and mathematical modeling will be able to response some of them.

Morgan et al. in 2009[15] made the first attempts to estimate the amount of produced ROS by X-PDT. Although many uncertainties existed in their simulations, it was a first attempt and raised valid questions about the practicality of X-PDT as an effective treatment option[9].

Bulin et al. in 2015[16] proposed an alternative model using GEANT4-based Monte Carlo simulations to numerically estimate the spatial energy distribution in a macroscopic volume of water loaded with nanoscintillators. The results showed at physiological NP concentrations, biological effects of radiation are primarily mediated by water, the most abundant molecule in biological tissues and absorption of energy by NPs is mainly driven by inelastic electron scattering and is nearly independent of the nanoparticle X-ray stopping power[9]. Following these results, Klein et al. in 2019[17] proposed a simplified electron cross section model to describe luminescence yield of NPs in a mix environment including water and nanoscintillators. They estimated that luminescence yield of NPs can be approximated as a function of the radiation dose, NP concentration, scintillator light yield and the electron cross-sections for tissue and the NP material. This model provides an upper bound for the actual number of scintillation photons emitted and is a better predictor of X-PDT efficacy. However, electron cross-section model as well as before theoretical models of X-PDT are not able to fully explain the X-PDT efficacy reported during pre-clinical tests[9]. The current models most predict the number of $^1O_2$ per cell over a wide excitation energy range, which is below the required 10^7 $^1O_2$ PDT threshold for cell killing. This is while experimental studies demonstrated that X-PDT is more than just a PDT derivative but it is essentially a PDT and RT combination[12]. Moreover, the current models of X-PDT most focused on the interaction of ionizing radiation with nanoscintillators and generated light with PSs to estimate $^1O_2$ concentration and predict produced $^1O_2$ based on some physical parameters such as radiation dosage, nanoscintillator concentration, scintillator light yield and tumor volume[15–18]. Indeed, none of them investigate effects of tumor microenvironment on the treatment efficiency while it is known that some chemical parameters like molecular oxygen has a significant impact on the success or failure of cancer treatments[19,20].

In the present study, we attempted to model cancerous cells treated with X-PDT through a feedback of tissue oxygen content. For this purpose, we first developed the mathematical model of tumor growth and then stablished a link between treatment parameters and physiological conditions of tumor environment. Due to the key role of molecular oxygen in RT effectiveness[21] and $^1O_2$ production in PDT[15], we do take care of oxygen and its dynamics as the main nutrient in tumor environment. We have developed a physicochemical model of X-PDT to incorporate molecular oxygen as one of the main factors determining the amount of produced ROS and also effectiveness of X-PDT[18]. In this regards, we considered a five compartment model (Fig. 1) including chemical transport, cancer cells dynamics, angiogenesis, blood flow and treatment models.

Results

Figure 2 shows initial results of the coupled model after the growth of 9 initial tumor cells includes (a) the tumor stages at the end of avascular growth phase after 41.6 days (b) inhibitor distribution produced randomly around the parent vessel as well as sprouts initiated from the center of each semi-circle (c) distribution of vessel radiuses and (d) oxygen production rates by the new microvessel structure after 141.6 days. According to the Fig. 2(a), tumor includes 3221 cells that 2304 quiescent cells placed at the internal layers and 917 proliferative cells at the external layer. Production of VEGF by the hypoxic tumor cells initiates angiogenesis process with sprouting 8 sprouts along the parent vessel and production of inhibitor around each new sprout (Fig. 2b). The activated
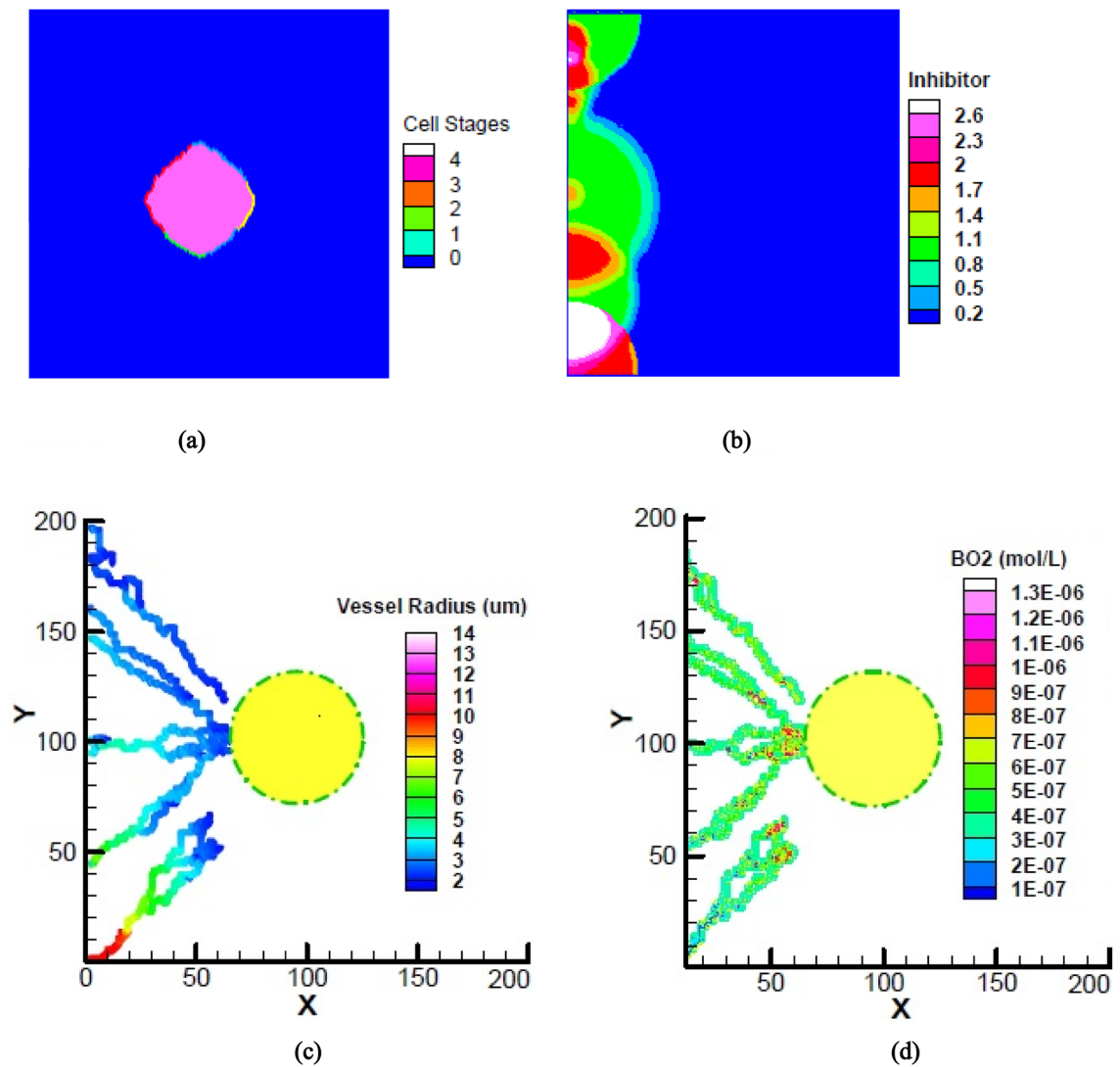
Figure 2. A snapshot of initial results of the coupled model includes: (**a**) tumor cell stages at the end of avascular growth phase (**b**) inhibitor distribution produced randomly around the parent vessel (**c**) vessel radius (**d**) Contribution of the produced capillary network in oxygen supply.

sprouts then move towards the VEGF source and form a new microvessel network to satisfy tumor cell demands. As shown in Fig. 2(c), the newly formed vessels have smaller diameters than the older ones (across x axis) and also vessel diameters vary depending on their positions along the parent vessel (across y axis) depending on the total applied stimulations S_{total}. Different branching patterns among 8 activated sprouts are also related to the various amount of S_{total} applied to each sprout tip. Contribution of new vessels in providing molecular oxygen is shown in Fig. 2(d) and illustrates that lower radiuses of vessel segments as well as more segment connections provide more oxygen to the tumor.

Figure 3 shows distribution of oxygen in tumor microenvironment after 141.6 days. In a vascularized tumor of Fig. 3(a), a mass of oxygen and other nutrients transferred by the new vessels in response to the VEGF produced by hypoxic tumor cells. On the other hand, in a non-vascularized tumor of Fig. 3(b), that angiogenesis is not initiated ($B_{O2}=0$), the lack of oxygen inside the tumor formed a layer of quiescent cells. The maximum level of oxygen in this situation corresponds to the minimum level of oxygen in the vascularized tumor of Fig. 3(a).

Now we investigate X-PDT efficiency for the two conditions of vascularized and non-vascularized tissue of Fig. 3. Figure 4 shows different cells of a vascularized tumor as well as normal tissue killed by $^1O_2$ during X-PDT with dose 4 Gy and nanocomplex concentration of 4 mg/ml. We assume that half of drug concentration remains in the adjacent normal tissue. As illustrated, cells in regions with higher oxygen concentrations targeted more effectively by $^1O_2$ both in tumor and normal tissue. According to the model considerations, new microvascular network initiated from the parent vessel on the left border of the domain, as a result cells in the left hand of the grid killed mostly by $^1O_2$. Based on these results, in this vascularized tumor, about 22.73% of tumor cells and 8.39% % of normal cells damaged due to $^1O_2$ toxicity. Among these, 2.54% of proliferative tumor cells (Fig. 4a) and 20.19% of quiescent tumor cells (Fig. 4b) have been damaged. Moreover, there is an isolated area inside the tumor where no cells have been killed and the treatment efficiency has been zero. Indeed, oxygen distribution
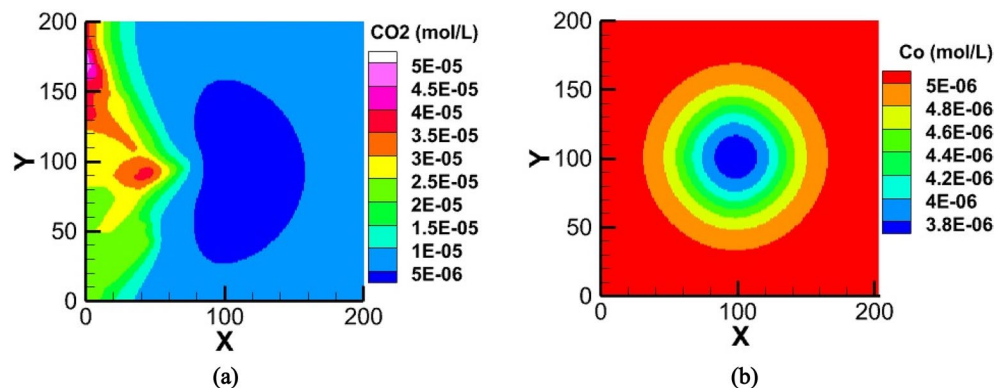
Figure 3. Distribution of oxygen in tumor and adjacent normal tissue, in a (**a**) vascularized tumor and (**b**) non-vascularized tumor.
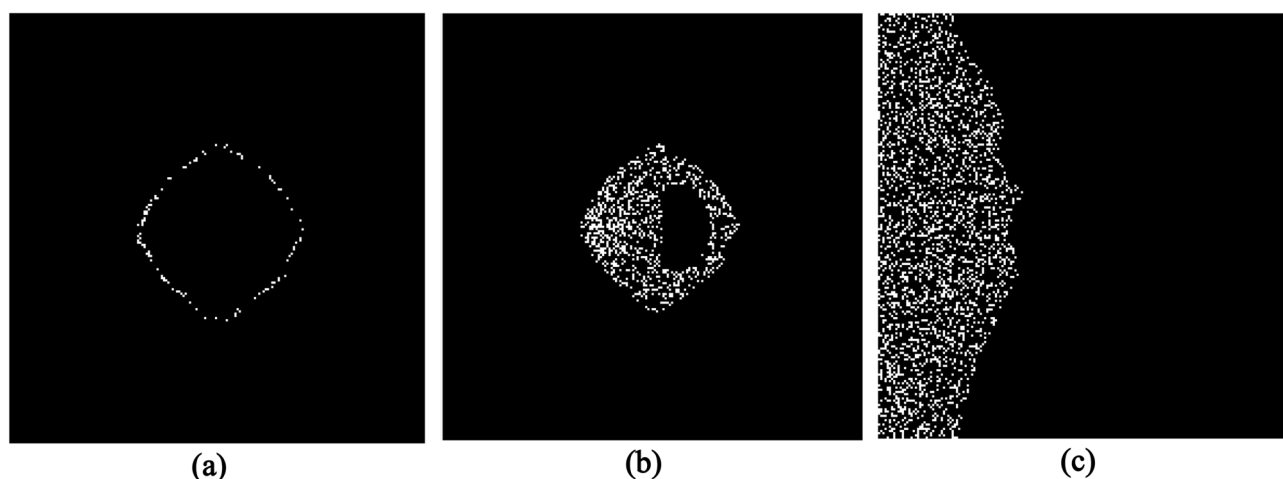

Figure 4. Proliferative (**a**) and quiescent (**b**) tumor cells as well as normal tissue (**c**) killed by $^1O_2$ during X-PDT in a vascularized tumor. The white spots in (**a**) & (**b**) are tumor cells and in (**c**) are normal cells. The black spots are background area in all.

determines the pattern of cell killing and hypoxia in this region acts like a defensive wall that protects tumor cells against $^1O_2$ toxicity. This isolated area is not necessarily placed in the center of the tumor but is placed in the region with minimum oxygen distribution. As well, the lack of oxygen in a non-vascularized tumor does not provide necessary $^1O_2$ threshold for cell killing. As a result, no tumor cells are destroyed by this X-PDT component in a non-vascularized tumor in the same condition.

Killing probability of $^1O_2$ in a vascularized and non-vascularized tumor under different tissue oxygen concentrations investigated in Fig. 5. As shown, killing probabilities depend quantitatively and qualitatively on the tissue oxygen level as well as tissue oxygenation properties. With increasing background oxygen concentration, probability of cell killing also increases both in vascularized and non-vascularized tumor, until the level of oxygen concentration is too high ($C_{O2} = 10\ C_{O2ref}$) that there is no difference between a vascularized and non-vascularized tumor in killing probability.

Tissue oxygenation properties also determine killing probabilities for tumor and adjacent normal tissue. As shown in Fig. 5, for a constant oxygen background concentration, killing probability differs depending on the tissue oxygenation conditions (Vascularized or non-vascularized). In a vascularized tissue, killing probability is distributed among different parts of the tumor (and normal tissue), while in a non-vascularized tissue different layers of tumor have almost similar killing probabilities. Moreover, in a non-vascularized tissue $^1O_2$ production is not sufficient to effectively destroy cancer cells except when tissue oxygen level becomes too high (Fig. 5b, d, f). It should be noted that in high oxygen levels ($C_{O2} = 10\ C_{O2ref}$), there is not high differences between the presence of a vascular network or not (Fig. 5e, f).

According to the results of Fig. 5, almost 50% of tumor cells will be killed by $^1O_2$ toxicity in sufficient oxygen concentration ($C_{O2} = 10\ C_{O2ref}$) in a vascularized tumor, but this is not all X-PDT efficiency because RT component will also target the cells, simultaneously. Figure 6 shows tumor and normal cells killed by RT in the presence of 4 mg/ml nanoscintillator concentration and radiation dose 4 Gy in a normal oxygen level (C_{O2ref}). According to the results, 37.26% of tumor cells killed by RT + RS that includes 3.59% proliferative cells and 33.67% quiescent cells. An interesting result is that the isolated area of tumor cells in Fig. 4(b) that $^1O_2$ failed to destroy them, now
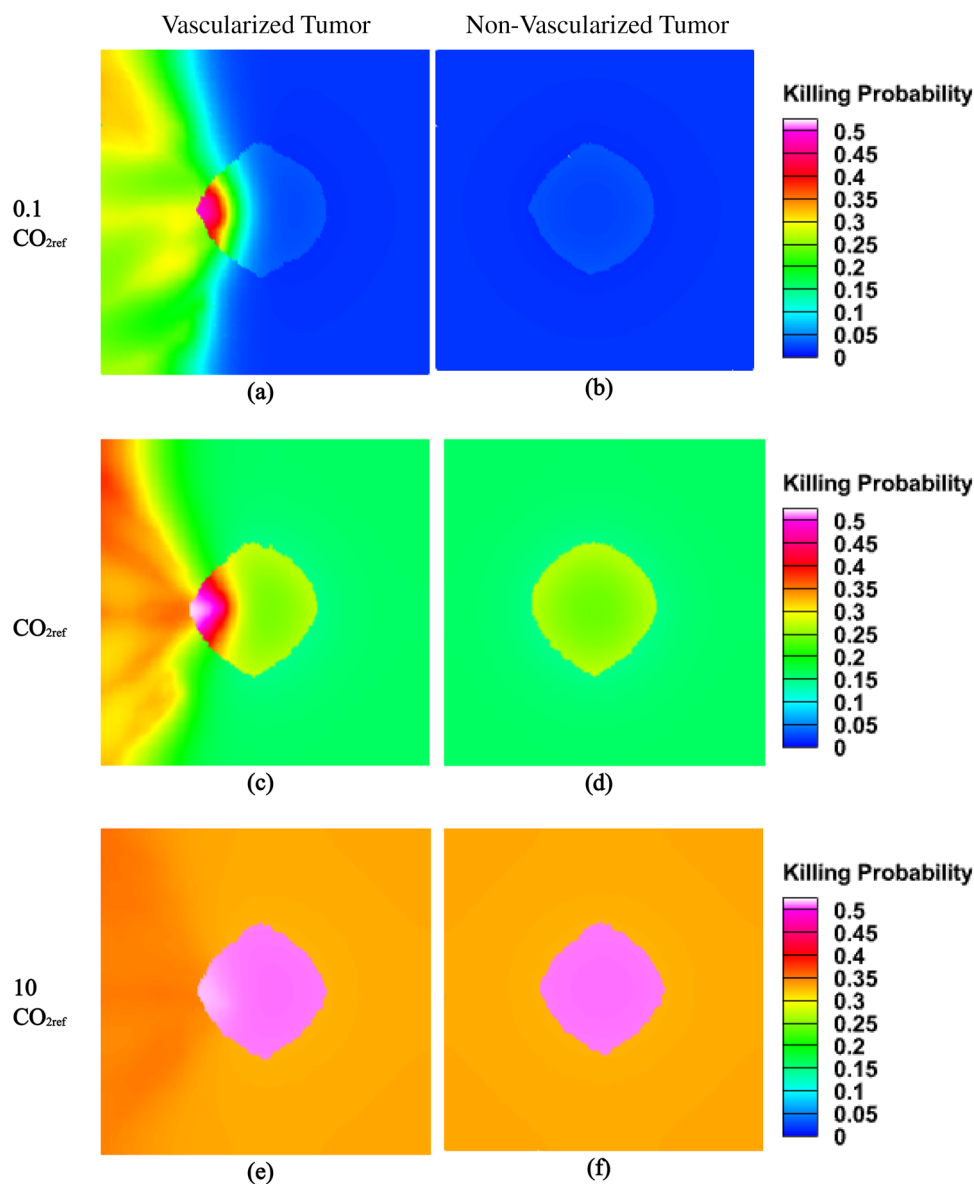
Figure 5. Probability of cell killing by $^1O_2$ during X-PDT in a vascularized and non-vascularized tissue as well as different tissue oxygen levels under dose 4 Gy and nanocomplex concentration of 4 mg/ml.

targeted by RT + RS component of X-PDT. Killing of tumor cells in these regions emphasize on the combination effects of RT and PDT components during X-PDT.

Figure 7 shows the efficiency of RT, RT + RS, PDT and X-PDT under different regimes of radiation doses and/or drug concentrations in a vascularized tumor with a constant oxygen concentration of CO_{2ref}. According to the results, RT alone (0–4 Gy) did not induce significant cell death, while RT in presence of radiosensitizers (RT + RS) increase cell death in drug concentrations of more than 2 mg/ml. PDT results estimate the amount of cell death happened due to $^1O_2$ production during X-PDT and X-PDT results summarize the total effects of RT + RS, $^1O_2$ toxicity and synergy effects of them, simultaneously. As shown, X-PDT is more effective than RT + RS and PDT alone at all doses and concentrations. As a comparison, in radiation dose of 4 Gy and drug concentration of 4 mg/ml, the cell viability dropped to 84.11% in RT only, 70.27% in PDT, 62.74% in RT + RS and 33.5 in X-PDT.

According to the Fig. 6(c), almost all of normal cells (98%) targeted by RT + RS in presence of 2 mg/ml nano-scintillator and radiation dose 4 Gy. Although most of surrounding normal cells are damaged, they are able to reconstruct themselves by cell repair mechanisms. Moreover, we assumed a strict situation that half of drug concentration remains in normal tissue under irradiation. However, treatment conditions include drug concentrations remain in healthy tissues should be optimization to reduce side effects. In pharmaceutical experiments, many efforts have been made to design ideal drug delivery systems so that drug loading in tumor cells with higher pH becomes more than normal low-pH tissues[22,23]. Figure 8 shows a moderately sensitive normal tissue and tumor cells before, just after and 4.16 days after X-PDT. Because DNA repair pathways of cancerous cells has been deregulated[24], they are unable to repair themselves (Fig. 8) as a result, in most cases, fractionated
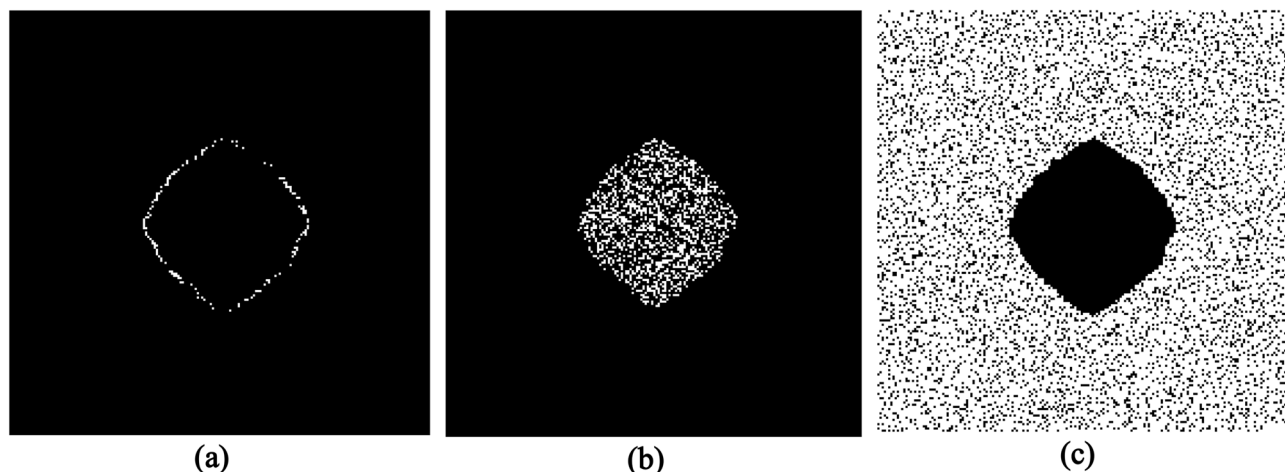
Figure 6. Different cells killed by RT + RS component of X-PDT includes (**a**) Proliferative and (**b**) Quiescent tumor cells as well as (**c**) Normal tissue. The white spots in (**a**) & (**b**) are tumor cells and in (**c**) are normal cells. The black spots are background area in all.
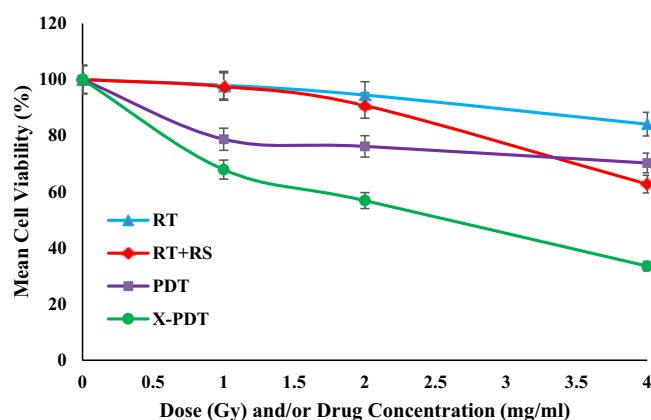

Figure 7. Comparison of mean tumor cell viability under different treatments of RT, RT + RS, PDT and X-PDT in a vascularized tumor with a constant tissue oxygen concentration of CO_{2ref}.

treatments lead to complete elimination of cancerous cells. In the current situation, although some of tumor cells (35.08%) still remains after the treatment (Fig. 8e), it is possible to omit remaining cells by applying a low dose RT alternately.

Figure 9 compares viability of tumor and normal cells under different X-PDT regimes. In comparison to the control group that receive RT only (C = 0 & D ≠ 0), cell viability decreases as NP concentration increases. Minimum cell viability of tumor equals to about 35.08% that is related to the NP concentration of 4 mg/ml and radiation dose 4 Gy (D = 4 & C = 4). Although increasing drug concentration compared to increasing radiation dose makes more reduction in tumor cell viability, this trend is opposite in normal cells. In other words, normal cells are more sensitive to changing in radiation doses compared to changes in NP concentration. Applying dose 4 Gy in all drug concentrations decreases normal cell viability below 20%, means that it is very toxic for them while the maximum reduction for tumor cells achieved in this dose and NP concentration 4 mg/ml. Therefore, it is a decision making problem to compromise between killing tumor cells and unwanted normal tissue side effects.

For better illustration, Tables 1 and 2 present percentages of tumor and normal cells killed by $^1O_2$ in a vascularized tissue under different oxygen concentrations and vascular network densities, respectively. Consulting the literature, we considered two reference values for tissue oxygen concentration (CO_{2ref}) and vessel branching age (ψ_{ref}) and compared the related results with the results in 0.25, 0.5, 2 and 4 times variations. According to the results, cell killing rate increases as tissue oxygen levels and microvascular network densities increase. Background oxygen concentration models inherent tissue differences in oxygen levels and we intended to predict why treatment efficiency differs among different cancers like colon compared to lung. Moreover, long-term effects of microvascular network densities appears in tissue oxygen levels. According to the simulations, when the tissue oxygen concentration increases to 4 $CO2_{ref}$, 46.47% of tumor cells killed due to $^1O_2$ toxicity that is 2 times larger than killing rate in CO_{2ref} condition. However, the rate of normal cell killing in this situation is more than 3 times compared to $CO2_{ref}$ situation. As a result, a high tissue oxygen level although increases tumor destruction, it simultaneously affect healthy tissue destruction more effectively. Thus, optimizing treatment conditions,
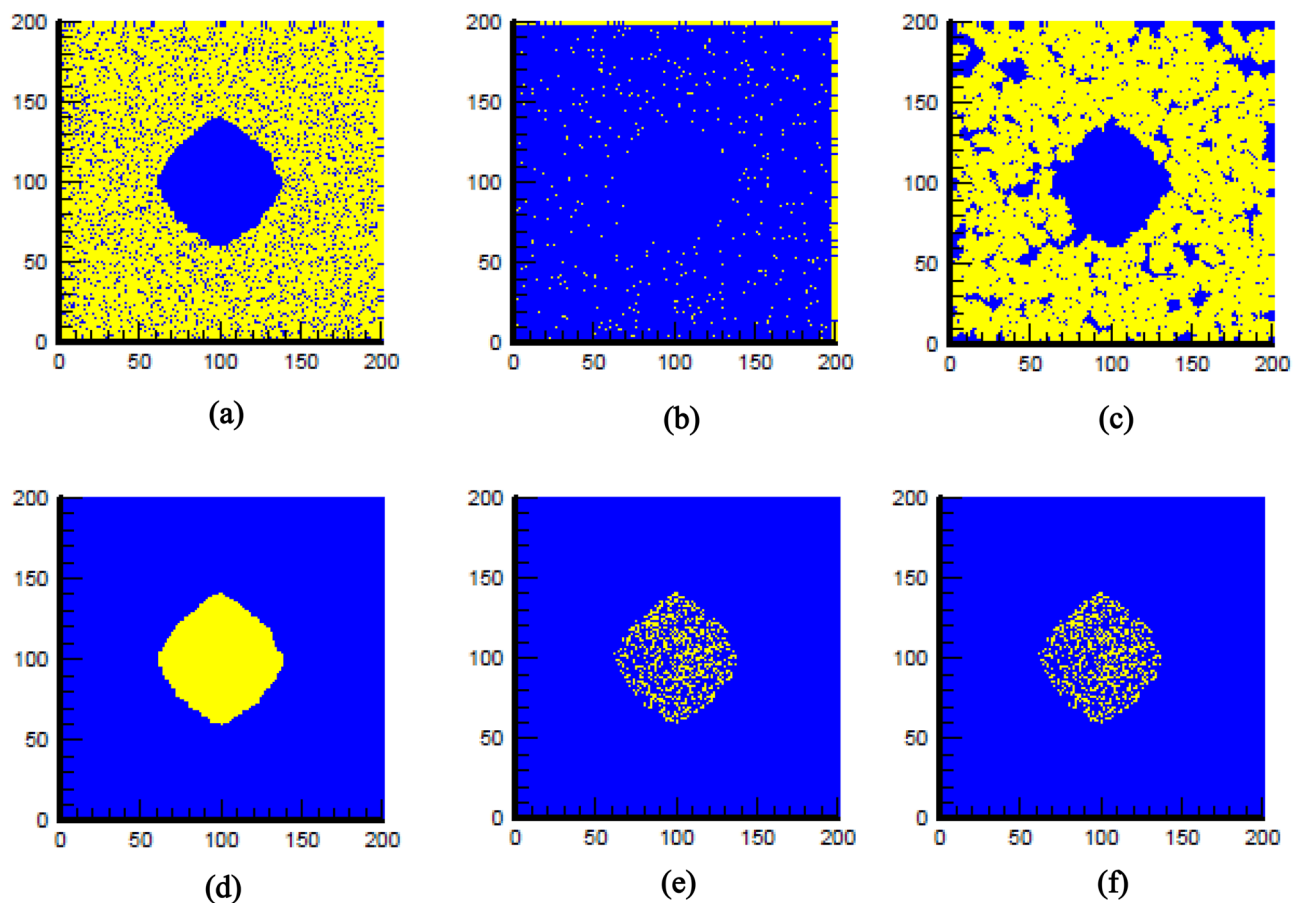
Figure 8. The results of X-PDT on a moderately sensitive normal tissue (**a-c**) as well as tumor cells (**d-f**) before (**a** & **d**), just after (**b** & **e**) and 4.16 days after X-PDT (**c** & **f**). The yellow color in the first row indicates normal cells and in the second row indicates tumor cells. The blue color in both rows shows the background area.
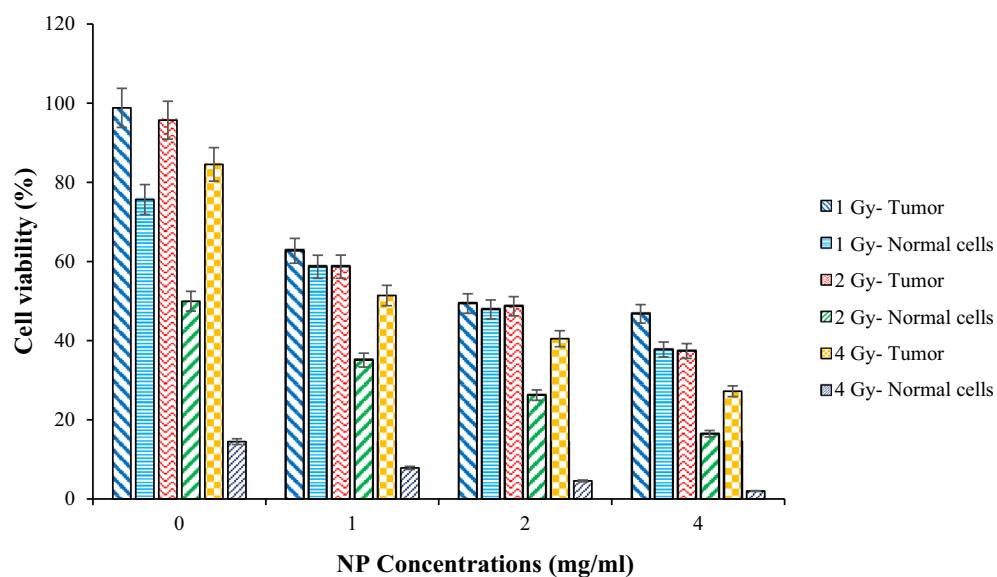

Figure 9. Comparison of tumor and normal cell viability under different X-PDT regimes with this assumption that half of these concentrations remains in adjacent normal tissue.

Tissue oxygen concentration (µmol/L)	Proliferative tumor cells	Quiescent tumor cells	Normal cells
CO2 = 0.65	1.03	4.94	7.71
CO2 = 2.6	0.9	6.17	8.83
CO2 = 5.2	2.54	20.19	8.39
CO2 = 10.4	3.90	34.32	11.16
CO2 = 20.8	4.41	42.06	28.42

Table 1. Percentages of different tumor cells and normal tissue killed by $^1O_2$ during X-PDT under various tissue oxygen concentrations in dose 4 Gy and NP concentration of 4 mg/ml.

Vessel branching age	Micro Vessel number (MVN)	Proliferative tumor cells	Quiescent tumor cells	Normal cells
$\psi = 0.25 \, \psi_{ref}$	1314	3.15	32.04	12.72
$\psi = 0.5 \, \psi_{ref}$	316	2.94	25.22	10.94
$\psi = \psi_{ref}$	53	2.54	20.19	8.39
$\psi = 2 \, \psi_{ref}$	21	2.47	18.27	8.80
$\psi = 4 \, \psi_{ref}$	14	2.52	17.66	7.79

Table 2. Percentages of different tumor cells and normal tissue killed by $^1O_2$ during X-PDT under various vascular network densities in dose 4 Gy and NP concentration of 4 mg/ml.

especially the amount of drug loading in tumor compared to healthy tissues, minimizes unwanted side effects. On the other hand, in a high density microvascular structure with $\psi = 0.25 \, \psi_{ref}$ that includes about 1314 vessel segments cells killed more effective than a network with $\psi = \psi_{ref}$ includes 53 vessel segments. Therefore, the results illustrate two important results should be considered in all $^1O_2$ based treatments include: (1) It should be considered a tradeoff between tumor cell reduction and normal tissue side effects and (2) tissue oxygen content as well as tissue oxygenation has an important role in treatment efficiency.

Discussion

In this paper, we considered available oxygen concentration in the vicinity of X-PDT drugs to evaluate production rate of singlet oxygen in tumor microenvironment. We also estimated cell killing probability in a vascularized and non-vascularized tissue for different levels of oxygen concentrations. Combination effects of RT in targeting the isolated cells escaping from PDT, emphasized that X-PDT is more than just a PDT derivative but it is essentially a PDT and RT combination[12]. Introducing physicochemical model of X-PDT with considering tissue oxygen concentration estimated killing rates in different tumor layers (proliferative and quiescent) and illustrated why some of the cells escape from $^1O_2$ toxicity. In this paper, we improved the existing models of X-PDT to investigate the effects of tissue oxygenation to find out the cause of different X-PDT outcomes in various tissues from the point of their oxygen content, although it did not greatly improve the number of produced $^1O_2$. Considering variable vessel diameters, cause to produce a more realistic vascular network in providing molecular oxygen. The results showed that death rates of the cells as well as mortality patterns depend on the tissue oxygen concentration and oxygenation properties such as micro vessel density. Hope that such studies have great importance to clinical applications of X-PDT in the near futures.

Mathematical modeling
Overview

Development of cancer begins with a mutation in certain key genes of a normal cell. One of this mutation results is cell's runaway from normal homeostatic mechanisms causing irregular cell proliferation. After a while, over successive divisions, a cluster of about 10^6 cancer cells forms that compete for space and nutrients. These new invading cells change the concentration of underlying molecules result in hypoxia at internal layers of tumor. Hypoxic cells secrete tumor angiogenic factors (TAFs) causing endothelial cells (EC), lining in nearby vessel walls, to form new blood vessels from the existing ones (angiogenesis)[25]. After triggering angiogenesis, blood flow penetrates into the network and provides oxygen and nutrients to the hypoxic cells. Angiogenesis process is a key feature of malignant tumors enables them to invade surrounding tissues (metastasis) and leads to challenges in their treatment. In the following, first we simulate growth of some initial tumor cells along with the consumption of chemicals include oxygen, glucose and hydrogen production to obtain appropriate concentration of molecules at the time of treatment. To model vascular tumor growth, we coupled our previous model[26] to the nutrient diffusion model[27] and estimate available tissue oxygen. Then, the edited model of X-PDT applied to estimate viability of cancerous cells through a feedback of tumor micro-environment. Details of each model explained in the following.

Chemical transport

We considered the key diffusible chemicals of oxygen, glucose, hydrogen ions and VEGF. Each tumor cell is assumed to consume nutrients (glucose and oxygen) and excrete metabolic waste (hydrogen). Tumor cells also secrete VEGF under hypoxic conditions. Differential equation describes the concentration of such molecules is[28]:

$$\frac{\partial C_i(x,y)}{\partial t} = D_i \nabla^2 C_i(x,y) + A_i + B_i \tag{1}$$

where $i = O_2, G, H$, denotes molecules of oxygen, glucose and hydrogen ion respectively. D_i are diffusion constants and functions A_i and B_i describe the consumption rate of molecules by the tumor cells and production rate of them by the vasculature, respectively. Also:

$$A_i = (W_i \phi) T_P \tag{2}$$

$$B_i = \sum \frac{2q_i}{R}(C_{b,i} - C_{w,i})E_{P,k} \tag{3}$$

where W_i is the uptake rate of molecule i by cancer cells, ϕ denotes the density of tumor cells, q_i is the vessel permeability to molecule i, R is microvessel radius, $C_{b,i}$ and $C_{w,i}$ are intravascular and wall concentrations of molecule i. Terms T_P and $E_{P,k}$ are Boolean indicators represent a tumor cell locating at node P and a capillary segment connecting node P with its neighboring nodes, respectively. The summation is taken over point P and its adjacent nodes ($k = N, S, W, E$).

For the simplicity, it is assumed that the intravascular concentrations of oxygen, glucose and hydrogen ions are preserved throughout the vasculature, so $C_{b,i}$ has a constant value. Finally, the interstitial VEGF transport equation is defined as[27]:

$$\frac{\partial C_v}{\partial t} = D_v \nabla^2 C_v + (W_v \phi)\eta_P - (\varepsilon_v \psi)\theta_P - \lambda_v C_v \tag{4}$$

where D_v is diffusion coefficient of VEGF, η_P and θ_P are Boolean indicators of the existence of hypoxic tumor cells and ECs on a grid point P, respectively, ε_v is take up rate of VEGF by ECs and λ_v is its natural decay rate.

Cell dynamics

This model consists of three different cell types includes tumor cells, normal tissue and vasculature. The internal metabolic activities of normal and tumor cells cover glycolysis, production of acid and oxidative phosphorylation[28]. Normal cells only proliferate if density of neighbors falls below a certain value (~ 80%) but tumor cells can proliferate until they fill all the available spaces[29]. We adopted the previously developed models of tumor metabolism to incorporate core metabolic activities of tumor and normal cells[27,29]. Using Michaelis–Menten kinetics, oxygen consumption W_o is determined by:

$$W_{O2}(x,y) = -V_{O2}\frac{C_{o2}(x,y)}{C_{o2}(x,y) + K_{O2}} \tag{5}$$

where $C_{O2}(x,y)$ is oxygen concentration, V_{O2} is maximum oxygen consumption and K_{O2} is the half maximum oxygen concentration. Glucose consumption is also driven by:

$$W_G(x,y) = -\left(\frac{P_G A_0}{2} + \frac{27 W_{O2}(x,y)}{10}\right)\frac{C_G(x,y)}{C_G(x,y) + K_G} \tag{6}$$

where $A_0 = \frac{29}{5}V_{O2}$ is the baseline production rate of ATP, and C_G and K_G are defined as glucose concentration, and half maximum concentration, respectively. The coefficient P_G is a multiplier representing the Warburg effect (i.e. altered glucose metabolism seen in many tumor cells) where $P_G = 1$ corresponds to normal glucose consumption, and $P_G > 1$ denotes more glucose consumption than needed to meet normal ATP demand. Defining the target ATP production rate as $\frac{W_A}{A_0}$, where:

$$W_A(x,y) = -\left(2 W_G(x,y) + \frac{27 W_{O2}(x,y)}{5}\right) \tag{7}$$

And

$$W_H(x,y) = K_H\left(\frac{29(P_G V_{O2} + W_{O2}(x,y))}{5}\right) \tag{8}$$

where parameter K_H accounts for proton buffering in the tumor microenvironment.

In the following, a set of cellular automaton (CA) rules are implemented into each cell to update its status in each time step (Fig. 10). One tumor cell per grid point is permitted either be a proliferating, quiescent, dead or treated ones. We developed some predefined rules[27] to incorporate progression of cells in cell cycle and model the effects of radiation cell cycle sensitivity[21]. Cell cycle is consisted of four stages: Mitosis (M), Gap1 (G1), Synthesis (S), and Gap2 (G2). In each stage, the cell undergoes a different process. During Mitosis, the cell divides
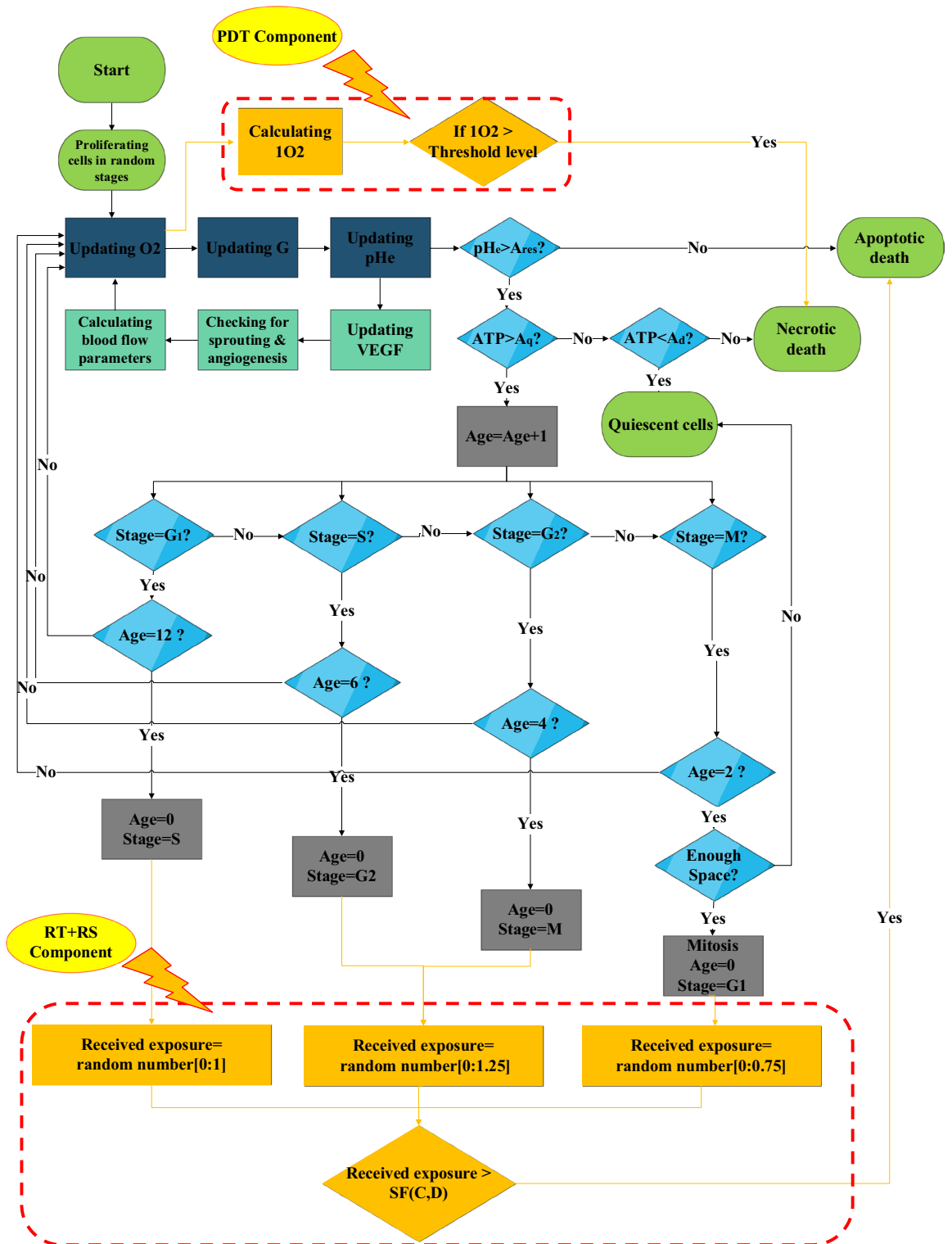
Figure 10. Model overview includes coupling of chemical diffusion model, cellular automaton rules and cancer cell dynamics. It is also shown how to get feedback from the model to apply the treatment at the desired time.

and produces two daughter cells. In G1 phase the cell increases in size and content. Throughout S phase DNA replication occurs and in G2 phase the cell continues to growth[30]. It is known that cells in G2 or mitosis stages are more sensitive to irradiation whereas cells in G1 stage are more resistant to radiation[31]. Figure 10 shows coupling of chemical diffusion model, cellular automaton rules, angiogenesis and blood flow model. It is also shown how to get a feedback from the tumor microenvironment to apply X-PDT components at the treatment time as will be discussed in the next sections.

Angiogenesis

The first step of angiogenesis is nearby vessel sprouting in response to factors secreted from hypoxic tumor cells (like VEGF). These sprouts then progress in extracellular matrix (ECM). Thus, two steps can be considered in angiogenesis modeling include sprouting and progression. To model sprouting, we use our previous model of adaptive sprout spacing (ASS) to estimate the number, position and time of activated sprouts along the parent vessel[26,32]. According this model, there are two conditions for sprouts to form: 1) If the concentration of activator around each point of the parent blood vessel become greater than or equal to a chosen trigger value, and 2) the inhibitor concentration at that point be less than or equal to a chosen inhibitor threshold value. Thus, If A and I denote the angiogenesis activator and inhibitor concentrations, respectively, the required conditions for sprouting will be formulated as:

$$A_l^q \geq A_{trigg,l}^q$$

$$I_l^q \leq I_{thresh,l}^q$$

where the subscripts specify the location on the grid and the superscripts specify the time steps.

Assuming that the activator is produced by hypoxic tumor cells, simply diffuses and decays. Inhibitor is also produced by each formed sprout and diffuses into the tissue around of it to inhibit formation of new sprouts with a random distance and then decays. Thus, the partial differential equations describing activator and inhibitor concentrations are as follows:

$$\frac{\partial A}{\partial t} = D_a \nabla^2 A - \lambda_a A \tag{9}$$

$$\frac{\partial I}{\partial t} = D_i \nabla^2 I - \lambda_i I \tag{10}$$

where D_a and D_i are activator and inhibitor diffusion coefficients, λ_a and λ_i are their decay rates, respectively, all taken as constants[33,34].

Activated sprouts then progress in ECM in three ways of random motility, chemotaxis and haptotaxis[35]. Three key variables considered for progression of activated sprouts include vascular endothelial growth factor (VEGF), fibronectin and ECs. The non-dimensional equation governing the distribution of ECs is defined as[35]:

$$\frac{\partial e}{\partial t} = \nabla . \left[D_e \nabla e - e \left(\frac{x}{1 + \sigma C_v} \nabla C_v + \rho \nabla f \right) \right] \tag{11}$$

where e, C_v and f denote non-dimensional endothelial cell density, VEGF and fibronectin concentrations, respectively. D_e, x and ρ are non-dimensional EC diffusion, chemotaxis, and haptotaxis coefficients, respectively. Using standard finite-difference methods, discretized form of the partial differential equations result in coefficients of the five-point finite-difference stencil to generate the probabilities of movement of an individual cell in response to its local milieu. The equation describing the interaction of sprouts with ECM fibers is:

$$\frac{\partial f}{\partial t} = \beta e - \gamma e f \tag{12}$$

where β and γ are positive constants expressing fibronectin production and proteolytic activity of EC tip, respectively. As the activated sprouts progress in ECM, they branch and anastomosis to form a novel capillary structure. Then blood flows in the hollow capillaries to supply tumor for chemicals. Moreover, the interaction of blood with capillary network remodel their structure via wall shear stress and upregulate microvessel radius.

Blood perfusion

Vascular network formed by angiogenesis model in previous section is a hollow network just determines the path of the endothelial cells. In order to estimate the amount of chemicals transferred by new vessels, blood flow analysis is required.

For non-Newtonian fluids, apparent viscosity μ_{app} is defined as the slope of the rheological curve at a specific shear rate. The well-known Poiseuille relation is applied to determine blood flow Q, while blood viscosity μ_{app} (R, H_D) is defined as a function of capillary radius and hematocrit. Assuming blood flow as an incompressible flow, then mass conservation equation is applied for all nodes of the network as:

$$\sum_{n=1}^{k} Q = 0 \tag{13}$$

When blood flows through a flexible vessel, resistance stresses will be generated depend on the vessel radius. On the other hand, when new vessels are forming, their radius can be determined depends on the entered shear stresses as:
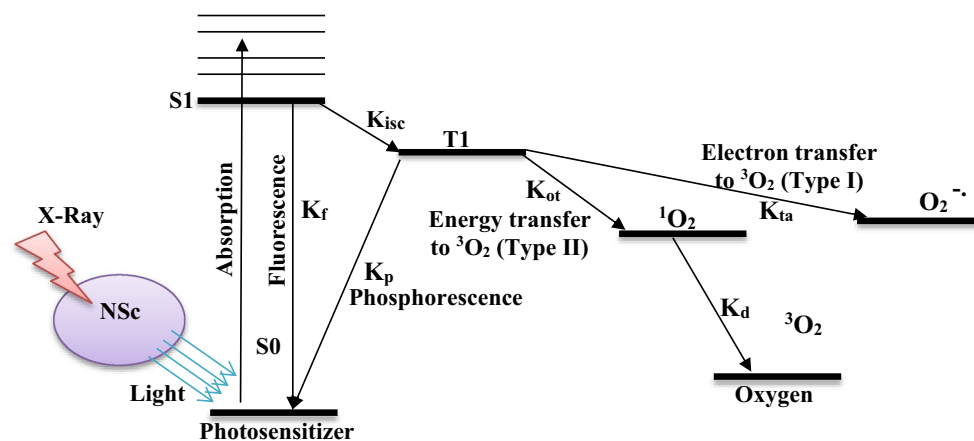
$$\Delta R = S_{total} R_{old} \Delta t \tag{14}$$

Figure 11. Photoactivation of photosensitizer during X-PDT by the light transmitted by nanoscintillator (NSc). $^1O_2$ formation in type II of PDT reactions are focused for modeling PDT component of X-PDT.

where Δt is the time step. We developed the chemical transport Eq. (3) to incorporate the effect of vessel diameter on the microvessel structure and amount of oxygen transferred by the novel network. Then, according to the amount of available oxygen and in the presence of specified concentrations of drug and radiation dose, cell viability will be computed. Therefore, Eq. (14) is used to update the new vessel radius as $R_{new} = R_{old} + \Delta R$. The total stimulus on a considered segment corresponds to the sum of each individual stimulus, S_{wss}, S_p, and S_m representing the wall shear stress, intravascular pressure, and metabolic stimulus, respectively as follows[36]:

$$S_{total} = S_{wss} + S_p + S_m \tag{15}$$

We used our previous algorithm of vessel adaptation[26] that employs an auxiliary function to predict network remodeling at specified future time steps. The updated network with new capillary radiuses, branches and flow parameters includes updated shear stresses, pressure differences and flow rates substituted with previous ones at each time step. Finally, production rates of molecules at new vascular network updated according to the new parameters.

Treatment model

Previous studies have experimentally demonstrated that X-PDT is essentially a PDT and RT combination[12]. The two modalities target different cellular components (cell membrane by PDT and DNA by RT), leading to enhanced therapy effects. The efficacy of X-PDT is therefore due to synergy effects of RT and PDT[37]. Current models have focused only on the singlet oxygen concentration to predict treatment efficiency of X-PDT and none of them considered RT component. In the following, we model the contribution of X-PDT components and investigate the role of tissue oxygen concentration and oxygenation properties in cell viabilities.

PDT component

Absorption of a photon by PS in its ground state, promotes it to a singlet excited state *S1* (Fig. 11). PS then lose its energy by emitting fluorescence and return to the ground state or transfer to a triplet state *T1* that has a longer lifetime. This process known as intersystem crossing (ISC) is an essential feature of a good PS. In the triplet state, PS may return to its ground state by emitting phosphorescence or transfer its energy to molecular oxygen (Type II) or transfer an electron to the biomolecules (Type I), which in subsequent reactions produces ROS[38].

Variable	Definition	Unit
S_0	Ground state photosensitizer concentration	mol L^{-1}
S_1	Single excited state photosensitizer concentration	mol L^{-1}
T1	triplet excited state photosensitizer concentration	mol L^{-1}
K_f	Decay rate of first excited single state photosensitizer to ground state photosensitizer	s
K_p	Decay rate of the photosensitizer triplet state	s
K_{isc}	Decay rate of first excited state photosensitizer to triplet state photosensitizer	s
K_{ot}	Biomolecular rate constant for reaction of $^3O_2$ with T1	mol L^{-1} s
K_{ta}	Biomolecular rate constant for reaction of T1 with biomolecules	mol L^{-1} s
K_d	Decay rate of first excited singlet oxygen to ground state triplet oxygen	s

Table 3. Parameter definitions and units of X-PDT process described in Fig. 11.

Molecular oxygen that is normally in the triplet state, converted to the $^1O_2$, during type II of PDT reactions. If the PS is not consumed in this process, the same PS molecule may create many singlet oxygen molecules. Parameter definitions and units of Fig. 11 are shown in Table 3.

For modelling PDT component, we focus on the production of $^1O_2$ as the dominant molecule during type II of PDT reactions. Because the dynamic processes of PDT are known to be very fast (~ μs or less)[38], the simplified equation of $^1O_2$ production in the time scale of a few seconds to hours, incorporates the mechanism developed by Georgakoudi et al.[39] and the corresponding X-PDT energy transfer mechanism proposed by Klein et al.[17] as:

$$C_{1O2} = N_{scint}\left[\frac{photons}{cm^3}\right] \times 1\left[\frac{1O2\,molecules}{photons}\right] \times \frac{C_{o2}(x,y)}{C_{o2}(x,y) + K_p/K_{ot}} \qquad (16)$$

Where N_{scint} is density of scintillation photons emitted by a dilute suspension of nanoscintillator and $C_{O2}(x,y)$ is oxygen concentrationin at the point (x,y). K_p is decay rate of triplet PS to the ground state and K_{ot} is the bimolecular rate of triplet PS quenching by $^3O_2$. We assume that all photons are converted to singlet oxygen molecules. N_{scint} describes energy transfer in X-PDT and depends on some physical parameters like radiation dosage d, nanoscintillator concentration C_{sc}, scintillator light yield Y_{sc} as[17]:

$$N_{scint}\left[\frac{photons}{cm^3}\right] = d\left[\frac{J}{kg}\right] \times 10^{-3}\left[\frac{kg}{g}\right] \times 6.2 \times 10^{12}\left[\frac{MeV}{J}\right] \times C_{sc}\left[\frac{g}{cm^3}\right]$$
$$\times \frac{(\mu/\rho)_{sc}[MeV \times cm^2 g^{-1}]}{(\mu/\rho)_{tissue}[MeV \times cm^2 g^{-1}]} \times Y_{sc}\left[\frac{photons}{MeV}\right] \qquad (17)$$

where μ/ρ is the electron cross-sections for tissue and the nanoscintillator material can be obtained from the ESTAR database, which is maintained by the National Institute of Standards and Technologies (NIST).

Finally, the corresponding number of $^1O_2$ production per cells (N_{1O2}) computed by multiplying the cell volume as:

$$N_{1O2}\left[\frac{1O2\,molecules}{cells}\right] = C_{1O2}\left[\frac{1O2\,molecules}{cm^3}\right] \times V_{cell}\left[\frac{cm^3}{cell}\right] \qquad (18)$$

Available molecular oxygen plays an important role in treatment efficiency so that quantum yield of $^1O_2$ is affected by the amount of oxygen consumption during X-PDT[19]. The physicochemical model of X-PDT can predict treatment failure at hypoxic tumor layers. However, for any (x,y) of the network if $C_{O2}(x,y) >> K_p/K_{ot}$, treatment efficiency depends only on the physical parameters of Eq. (17). As well, if $C_{O2}(x,y) << K_p/K_{ot}$, production rate of $^1O_2$ is concerned by oxygen content of tissue, leading to unpredictable treatment effect[40,41]. Therefore, the correspondence between the oxygen content of the tissue and the selected photosensitizer can be effective in treatment efficiency. In this regards, the oxygen content of the tissue for a specific photosensitizer in different states of presence or absence of a vascular network, as well as different tissue oxygen levels, has been investigated in the results.

Estimation of compensation coefficient
Proposed physicochemical model of X-PDT by considering oxygen concentration may not greatly improve the number of produced $^1O_2$, but it could illustrate dependence of $^1O_2$ yield to the available molecular oxygen. Therefore, in order to model cellular death caused by $^1O_2$, we used invers engineering to compute the required coefficient for compensating the lack of $^1O_2$ number from the lethal threshold value 4×10^7 reported by Neider et al.[42]. We assume this compensation coefficient η_c represents all the factors that is predicted in experimental observations but have not yet been considered in modelling. Some of these factors include non-optical forms of energy transfer between nanoscintillator and conjugated photosensitizers[9], catalyzing the radiation-induced formation of radicals and ROS by NPs[43], enhancing radiation dose within nanometers of NP surfaces[44]. The role of all these factors applied by product a compensation coefficient η_c in Eq. (18).

RT component
As mentioned before, each nanocomposite used in X-PDT contains a nanoscintillator and some conjugated PSs. While nanoscintillator is a light source for PS, it has also some radiation sensitizing properties[11]. In this part, we consider the effects of radiation at existence of nanoscintillators. Using nanoscintillators (radiosensitizers) can have many different mechanisms of action on effective killing of cancerous cells and improvement of treatment efficiency. Cardilin et al.[6] proposed a model based on LQ theory and lump all of radiosensitizer processes together as having the net action of linear stimulating the radiation-induced mass transfer to make the model generally applicable. According to this model, the proportion of cancer cells surviving an irradiation dose d and plasma concentration of the radiosensitizer C equals to:

$$SF(C,d) = exp[-(1+bC)(\alpha d + \beta d^2)] \qquad (19)$$

where α (Gy^{-1}) and β (Gy^{-2}) are cell-specific radiosensitivity parameters and b is a pharmacodynamic parameter associated with the radiosensitizing effects.

We call this part of X-PDT as "RT + RS component" and couple this linear stimulatory function with the tumor growth model as shown in Fig. 10 in order to estimate this component of X-PDT at the time of treatment. We also consider cell cycle sensitivity under irradiation[21] and investigate a moderately sensitive normal tissue with

Parameter	Description	Value	Unit	References
P_G	Upregulated glucose uptake rate	1	–	[27]
α	Probabilities of double-strand breaks in DNA of tumor cells	0.002	G^{-1}	Estimated
β	Probabilities of radiation repair of tumor cells	0.01	G^{-2}	Estimated
α_NC	Probabilities of double-strand breaks in DNA of normal cells	0.211	G^{-1}	[48]
β_NC	Probabilities of radiation repair of normal cells	0.068	G^{-2}	[48]
Y_{sc}	Light yield of scintillator	10^5	Photons/MeV	[17]
D_{O2}	Tissue oxygen diffusivity	2.41×10^{-5}	$cm^2\ s^{-1}$	[49]
K_{O2}	Half-max O_2 concentration	5×10^{-6}	$mol\ L^{-1}$	[29]
V_{O2}	Max O_2 consumption	2.3×10^{-16}	$mol\ (cell\ s)^{-1}$	[50]
D_G	Tissue glucose diffusivity	9×10^{-5}	$cm^2\ s^{-1}$	[51]
D_H	Tissue hydrogen ion diffusivity	1.1×10^{-5}	$cm^2\ s^{-1}$	[51]
K_G	Half-max glucose concentration	4×10^{-5}	$mol\ L^{-1}$	[29]
K_H	Proton buffering coefficient	2.5×10^{-4}	–	[28]
A_{res}	pH Cancer cell acid resistance	6	pH	[52]
A_d	ATP Threshold for death	0.3	–	[28]
A_q	ATP Threshold for quiescence	0.8	–	[28]
b	Pharmacodynamic parameter associated with the radiosensitizing effect	0.45	ml/mg	[6]
$C_{b,o2}$	Intravascular concentration of oxygen	5.6×10^{-5}	$mol\ L^{-1}$	[28]
$C_{b,g}$	Intravascular concentration of glucose	5×10^{-3}	$mol\ L^{-1}$	[27]
$C_{b,H2}$	Intravascular concentration of acid	3.98×10^{-8}	$mol\ L^{-1}$	[51]
ψ_{ref}	Threshold of vessel branching age	18	hr	[35]
K_p/K_{ot}	The ratio of the monomolecular decay rate of the triplet state photosensitizer to the biomolecular rate of the triplet photosensitizer quenching by $^3O_2$	11.9×10^{-6} (PpIx)	$mol\ L^{-1}$	[39]
ϕ	Density of tumor cells	5×10^7	$cells\ cm^{-3}$	Calculated

Table 4. Parameter values selected for mathematical modeling.

$\alpha/\beta = 3.1$[45] to estimate treatment side effects. Moreover, we assume that normal cells have the ability to repair damages caused by radiation while the repair pathways in tumor cells is demolished due to mutation[46].

Initial and boundary conditions
Simulations were carried out on a 200×200 grid, which is a discretization of the unit square $[0, 1]\times[0, 1]$, with a space step of h = 0.005, representing a tissue with dimensions of 5 mm × 5 mm. Consulting the literature a grid size of $\Delta x = \Delta y = 25\ \mu m$ was set which corresponds to the approximate size of a tumor cell[47]. We initiallly assume 9 proliferative tumor cells with random stages and appropriate ages placed at the center of the domain. The rest of the lattice space is filled by normal cells with a density of 80%. A parent vessel is lining on the left border of the domain. Initial pH value of the tumor microenvironment is set to 7.4. Initial concentrations of 5.2×10^{-6} mol/L and 5×10^{-3} mol/L are set for oxygen and glucose, respectively[27]. Also, the nodal pressure difference of blood in preexisting vessels is set to $\Delta P = 100$ mmHg with the radius of 14 μm. All capillary segments are assumed to be of initial radius and length of 2 μm and 25 μm, respectively. No flux boundary conditions are adopted for the interstitial diffusion equations. Other required parameter values are given in Table 4.

Data availability
All data generated or analyzed during this study are included in this published article.

References
1. Stamatakos, G. S., Dionysiou, D. D., Zacharaki, E. I. & Mouravliansky, N. A. In silico radiation oncology: Combining novel simulation algorithms with current visualization techniques. *Proc. IEEE.* **90**, 1764–1777 (2002).
2. Mladenov, E., Magin, S., Soni, A. & Iliakis, G. DNA double-strand break repair as determinant of cellular radiosensitivity to killing and target in radiation therapy. *Front. oncol.* **3**, 113 (2013).
3. Forastiere, A. A. *et al.* Concurrent chemotherapy and radiotherapy for organ preservation in advanced laryngeal cancer. *N. Engl. J. Med.* **349**, 2091–2098 (2003).
4. Hendee, W. R., Ibbott, G. S. & Hendee, E. G. *Radiation Therapy Physics* (Wiley, 2013).
5. Juzenas, P. *et al.* Quantum dots and nanoparticles for photodynamic and radiation therapies of cancer. *Adv. Drug Deliv. Rev.* **60**, 1600–1614 (2008).
6. Cardilin, T. *et al.* Model-based evaluation of radiation and radiosensitizing agents in oncology. *CPT Pharmacometrics Syst Pharmacol.* **7**, 51–58 (2018).
7. Dolmans, D. E., Fukumura, D. & Jain, R. K. Photodynamic therapy for cancer. *Nat. Rev. Cancer.* **3**, 380–387 (2003).
8. Wang, Y. *et al.* Ordered nanoporous silica as carriers for improved delivery of water insoluble drugs: A comparative study between three dimensional and two dimensional macroporous silica. *Int. J. Nanomed.* **8**, 4015 (2013).

9. Sun, W., Zhou, Z., Pratx, G., Chen, X. & Chen, H. Nanoscintillator-mediated x-ray induced photodynamic therapy for deep-seated tumors: From concept to biomedical applications. *Theranostics.* **10**, 1296 (2020).
10. Mulder, W. J. *et al.* Nanoparticulate assemblies of amphiphiles and diagnostically active materials for multimodality imaging. *Acc. Chem. Res.* **42**, 904–914 (2009).
11. Mesbahi, A. A review on gold nanoparticles radiosensitization effect in radiation therapy of cancer. *Rep Pract Oncol Radiother.* **15**, 176–180 (2010).
12. Wang, G. D. *et al.* X-ray induced photodynamic therapy: A combination of radiotherapy and photodynamic therapy. *Theranostics.* **6**, 2295 (2016).
13. Halliwell, B. & Gutteridge, J. M. Oxygen free radicals and iron in relation to biology and medicine: Some problems and concepts. *Arch. Biochem. Biophys.* **246**, 501–514 (1986).
14. Chen, W. & Zhang, J. Using nanoparticles to enable simultaneous radiation and photodynamic therapies for cancer treatment. *J. Nanosci. Nanotechnol.* **6**, 1159–1166 (2006).
15. Morgan, N. Y., Kramer-Marek, G., Smith, P. D., Camphausen, K. & Capala, N. Nanoscintillator conjugates as photodynamic therapy-based radiosensitizers: Calculation of required physical parameters. *Radiat. Res.* **171**, 236–244 (2009).
16. Bulin, A.-L. *et al.* Modelling energy deposition in nanoscintillators to predict the efficiency of the X-ray-induced photodynamic effect. *Nanoscale.* **7**, 5744–5751 (2015).
17. Klein, J. S., Sun, C. & Pratx, G. Radioluminescence in biomedicine: Physics, applications, and models. *Phys. Med. Biol.* **64**, 04TR01 (2019).
18. Clement, S., Deng, W., Camilleri, E., Wilson, B. C. & Goldys, E. M. X-ray induced singlet oxygen generation by nanoparticle-photosensitizer conjugates for photodynamic therapy: Determination of singlet oxygen quantum yield. *Sci. Rep.* **6**, 1–9 (2016).
19. Liu, T. *et al.* Method for monitoring singlet oxygen quantum yield in real time by time resolved spectroscopy measurement. *Opt. Express.* **28**, 25757–25766 (2020).
20. Zhu, T. C., Parsai, E. I. & Orton, C. G. PDT is better than alternative therapies such as brachytherapy, electron beams, or low-energy x rays for the treatment of skin cancers. *Med. Phys.* **38**, 1133–1135 (2011).
21. Jalalimanesh, A., Haghighi, H. S., Ahmadi, A., Hejazian, H. & Soltani, M. Multi-objective optimization of radiotherapy: Distributed Q-learning and agent-based simulation. *J. Exp. Theor. Artif. Intell.* **29**, 1071–1086 (2017).
22. Vejdani Noghreiyan, A. V., Photodynamic activation of silica/TiO₂/PpIX nanostructure by X-rays and its evaluation on survival of the human melanoma and colon cell lines. In *Mashad University of Medical Sciences*. Mashad University of Medical Sciences, School of Medicine. p. 138 (2020).
23. Bakhshizadeh, M. *et al.* Utilizing photosensitizing and radiosensitizing properties of TiO2-based mitoxantrone imprinted nano-polymer in fibrosarcoma and melanoma cells. *Photodiagnosis Photodyn. Ther.* **25**, 472–479 (2019).
24. Li, L., Guan, Y., Chen, X., Yang, J. & Cheng, Y. DNA repair pathways in cancer therapy and resistance. *Front. Pharmacol.* **11**, 2520 (2021).
25. Folkman, J. & Klagsbrun, M. Angiogenic factors. *Science.* **235**, 442–447 (1987).
26. Naghavi, N., Hosseini, F. S., Sardarabadi, M. & Kalani, H. Simulation of tumor induced angiogenesis using an analytical adaptive modeling including dynamic sprouting and blood flow modeling. *Microvasc. Res.* **107**, 51–64 (2016).
27. Shamsi, M., Saghafian, M., Dejam, M. & Sanati-Nezhad, A. Mathematical modeling of the function of Warburg effect in tumor microenvironment. *Sci. Rep.* **8**, 1–13 (2018).
28. Robertson-Tessi, M., Gillies, R. J., Gatenby, R. A. & Anderson, A. R. A. Impact of metabolic heterogeneity on tumor growth, invasion, and treatment outcomes. *Cancer Res.* **75**, 1567–1579 (2015).
29. Ibrahim-Hashim, A. *et al.* Defining cancer subpopulations by adaptive strategies rather than molecular properties provides novel insights into intratumoral evolution. *Cancer Res.* **77**, 2242–2254 (2017).
30. Cooper, G. M. & Hausman, R. *The Cell. A molecular approach* 2nd edn. (Sinauer Associates, 2000).
31. Joiner, M. C., Kogel, A. J. & Steel G. G. Introduction: The significance of radiobiology and radiotherapy for cancer treatment. In *Basic Clinical Radiobiology* (CRC Press, 2009).
32. Hosseini, F. & Naghavi, N. Modelling tumor-induced angiogenesis: Combination of stochastic sprout spacing and sprout progression. *J. Biomed. Phys. Eng.* **7**, 233 (2017).
33. Addison-Smith, B., McElwain, D. L. S. & Maini, P. K. A simple mechanistic model of sprout spacing in tumour-associated angiogenesis. *J. Theor. Biol.* **250**, 1–15 (2008).
34. Anderson, A. R. A., Chaplain, M. A. J., Garcia-Reimbert, C. & Vargas, C. A. A gradient-driven mathematical model of antiangiogenesis. *Math Comput Model Dyn Syst.* **32**, 1141–1152 (2000).
35. Anderson, A. R. & Chaplain, M. A. Continuous and discrete mathematical models of tumor-induced angiogenesis. *Bull. Math. Biol.* **60**, 857–899 (1998).
36. Stéphanou, A., McDougall, S. R., Anderson, A. R. & Chaplain, M. A. Mathematical modelling of the influence of blood rheological properties upon adaptative tumour-induced angiogenesis. *Math Comput Model Dyn Syst* **44**, 96–123 (2006).
37. Bulin, A.-L., Broekgaarden, M., Simeone, D. & Hasan, T. Low dose photodynamic therapy harmonizes with radiation therapy to induce beneficial effects on pancreatic heterocellular spheroids. *Oncotarget.* **10**, 2625 (2019).
38. Kim, M. M., Ghogare, A., Greer, A. & Zhu, T. C. On the in vivo photochemical rate parameters for PDT reactive oxygen species modeling. *Phys. Med. Biol.* **62**, R1 (2017).
39. Georgakoudi, I., Nichols, M. G. & Foster, T. H. The mechanism of Photofrin photobleaching and its consequences for photodynamic dosimetry. *Photochem. Photobiol.* **65**, 135–144 (1997).
40. Li, M. *et al.* Unimolecular photodynamic O2-economizer to overcome hypoxia resistance in phototherapeutics. *J. Am. Chem. Soc.* **142**, 5380–5388 (2020).
41. Shao, Y. *et al.* Engineering of upconverted metal–organic frameworks for near-infrared light-triggered combinational photodynamic/chemo-/immunotherapy against hypoxic tumors. *J. Am. Chem. Soc.* **142**, 3939–3946 (2020).
42. Niedre, M. J., Secord, A., Patterson, M. S. & Wilson, B. C. In vitro tests of the validity of singlet oxygen luminescence measurements as a dose metric in photodynamic therapy. *Cancer Res.* **63**, 7986–7994 (2003).
43. Sicard-Roselli, C. *et al.* A new mechanism for hydroxyl radical production in irradiated nanoparticle solutions. *Small.* **10**, 3338–3346 (2014).
44. Retif, P. *et al.* Nanoparticles for radiation therapy enhancement: The key parameters. *Theranostics.* **5**, 1030 (2015).
45. Zhang, H., Zhong, H., Barth, R. F., Cao, M. & Das, I. J. Impact of dose size in single fraction spatially fractionated (grid) radiotherapy for melanoma. *Med phys.* **41**, 021727 (2014).
46. Li, L. Y., Guan, Y. D., Chen, X. S., Yang, J. M. & Cheng, Y. DNA repair pathways in cancer therapy and resistance. *Front. Pharmacol.* **11**, 629266 (2021).
47. Anderson, A. R. A hybrid mathematical model of solid tumour invasion: The importance of cell adhesion. *Math Med Biol.* **22**, 163–186 (2005).
48. Withers, H. R. *et al.* Late normal tissue sequelae from radiation therapy for carcinoma of the tonsil: Patterns of fractionation study of radiobiology. *Int. J. Radiat. Oncol. Biol. Phys.* **33**, 563–568 (1995).
49. Goldman, D. & Popel, A. S. A computational study of the effect of capillary network anastomoses and tortuosity on oxygen transport. *J. Theor. Biol.* **206**, 181–194 (2000).

50. Molter, T. W. *et al.* A new approach for measuring single-cell oxygen consumption rates. *IEEE Trans Autom Sci Eng.* **5**, 32–42 (2008).
51. Gatenby, R. A. & Gawlinski, E. T. The glycolytic phenotype in carcinogenesis and tumor invasion: Insights through mathematical models. *Cancer Res.* **63**, 3847–3854 (2003).
52. Patel, A. A., Gawlinski, E. T., Lemieux, S. K. & Gatenby, R. A. A cellular automaton model of early tumor growth and invasion: The effects of native tissue vascularity and increased anaerobic tumor metabolism. *J. Theor. Biol.* **213**, 315–331 (2001).

Author contributions

F.S.H. conceived, designed and performed the simulations and data analysis. She also wrote the manuscript and interpret the results. N.N. reviewed the manuscript, interpret and approved the results. A.S. advised the work and reviewed the manuscript.

Competing interests

The authors declare no competing interests.

Additional information

Correspondence and requests for materials should be addressed to N.N.

Reprints and permissions information is available at www.nature.com/reprints.

Publisher's note Springer Nature remains neutral with regard to jurisdictional claims in published maps and institutional affiliations.